Electronic structure of fully epitaxial Co_2TiSn thin films

Markus Meinert,* Jan Schmalhorst, Hendrik Wulfmeier, and Günter Reiss
Thin Films and Physics of Nanostructures, Department of Physics, Bielefeld University, D-33501 Bielefeld, Germany

Elke Arenholz
Advanced Light Source, Lawrence Berkeley National Laboratory, Berkeley, California 94720, USA

Tanja Graf and Claudia Felser
Institute of Inorganic Chemistry and Analytical Chemistry, Johannes Gutenberg University, D-55128 Mainz, Germany
(Received 28 October 2010; published 15 February 2011)

We report on the properties of thin films of the full Heusler compound Co_2TiSn prepared by dc magnetron co-sputtering. Fully epitaxial, stoichiometric films were obtained by deposition on MgO (001) substrates at substrate temperatures above 600 °C. The films are well ordered in the $L2_1$ structure, and the Curie temperature slightly exceeds the bulk value. They show a significant, isotropic magnetoresistance and the resistivity becomes strongly anomalous in the paramagnetic state. The films are weakly ferrimagnetic, with nearly 1 μ_B on the Co atoms, and a small antiparallel Ti moment, in agreement with theoretical expectations. From comparison of x-ray absorption spectra on the Co $L_{3,2}$ edges, including circular and linear magnetic dichroism, with *ab initio* calculations of the x-ray absorption and circular dichroism spectra we infer that the electronic structure of Co_2TiSn has essentially nonlocalized character. Spectral features that have not been explained in detail before are explained here in terms of the final-state band structure.

DOI: 10.1103/PhysRevB.83.064412 PACS number(s): 75.70.−i, 78.70.Dm, 73.61.At, 81.15.Cd

I. INTRODUCTION

The materials class of Co_2YZ Heusler compounds (with Y a transition metal and Z an *sp* element) has been the subject of extensive studies in the context of spintronics during the last decade. They are of interest because many of them are predicted as half-metallic ferromagnets with full spin polarization at the Fermi edge.

The Heusler compound Co_2TiSn (CTS) is of particular interest for applications. It is predicted to be a half-metallic ferrimagnet with a magnetic moment of 2 μ_B/f.u. and it has a high formation energy of the Co-Ti site-swap defect.[1,2] Making use of Heusler compounds which exhibit low disorder or high tolerance of the ground-state properties against disorder is highly desired.

Co_2TiSn has been the subject of many experimental and theoretical studies. The ground-state properties obtained by density functional theory (DFT) depend sensitively on the choice of the DFT method.[1–8] The potential has strong non-spherical components and thus only a full-potential treatment in connection with the generalized gradient approximation (GGA) to the density yields a half-metallic ground state.[1,4]

Experiments conducted on bulk CTS find a lattice parameter of 6.07 Å, a magnetic moment of about 1.95 μ_B/f.u., and a Curie temperature (T_C) around 355 K.[1,9,10] Furthermore, it is found to have a strongly anomalous temperature dependence of resistivity; the temperature coefficient becomes negative above the Curie temperature. A large negative magnetoresistance reveals the importance of spin fluctuations in the compound.[11]

A rather new development aims at the magnetocaloric properties of Co_2TiSn, which has a large and constant Seebeck coefficient of -50 μV/K above T_C in the bulk.[10] There have been some efforts to understand the unusual transport properties of CTS by *ab initio* band structure and semiclassical transport theory.[10,12] These properties make CTS interesting for a possible application in spin caloritronics, which attempts to make use of the interactions between heat and spin. An implementation into thin films is of particular importance for such applications.

Only two studies on thin films of CTS are available as far as we know. Gupta *et al.* applied pulsed laser ablation to grow CTS on Si (001) substrates from a stoichiometric target at growth temperatures up to 200 °C.[13] The authors found off-stoichiometric, polycrystalline films with (022) texture. Suharyadi *et al.* utilized an atomically controlled alternate deposition technique based on electron-beam evaporation.[14] They grew (001) oriented, $L2_1$-ordered films on Cr-buffered MgO (001) substrates at growth temperatures up to 600 °C and investigated them by nuclear resonant scattering.

In this article, we present a successful preparation technique based on dc magnetron co-sputtering. We present data on the structural and magnetic properties of our films. Furthermore, we characterize the electronic transport properties that make CTS a particularly interesting compound. Finally, we discuss the electronic structure of our CTS films based on soft x-ray absorption spectroscopy and *ab initio* electronic structure calculations.

A. Experimental details

The samples were deposited using a UHV sputtering system equipped with five dc and two rf 3-in. magnetron sputtering sources arranged in a confocal sputter-up geometry. Material can be deposited from up to four sources simultaneously. The target-to-substrate distance is 21 cm and the inclination of the sources is 30°. The substrate can be rotated at 30 rpm and heated to 1000 °C by a ceramic heater via radiation from the substrate carrier backside. The deposition process can be controlled with an *in situ* quartz film thickness monitor, which can be moved to the position where the substrate is located

during deposition. Moreover, an electron-beam evaporator with one crucible is placed in the center of the chamber. Film thickness homogeneity is better than ±5% over a substrate diameter of 4 in. for sputtering as well as evaporation with rotation turned on. The base pressure of the system is typically better than 3×10^{-9} mbar.

Using the quartz sensor and x-ray reflectometry (XRR), the film stoichiometry of a compound can be set up with a relative accuracy of about ±10%. Using inductively coupled plasma optical emission spectroscopy (ICP-OES) the sputter parameters were fine-tuned. For the samples deposited at high temperature we checked the stoichiometry by energy dispersive x-ray analysis (EDX) in an electron microscope and found no deviation from the stoichiometry of room temperature deposited films of same thickness. The sputtering power ratios were 1:1.67:0.34 (Co:Ti:Sn). The voltages were constantly monitored during the deposition, which remained constant throughout all deposition processes, ensuring the reproducibility of the method. Crosstalk effects on the Sn target constituted a serious problem for the deposition process due to the low sputtering power applied to the source. This was suppressed by a chimneylike cylinder put around the source, such that there was no line of sight from this target to another. The compound was deposited at a rate of 1.5 Å/s. Sample rotation was set to 28 rpm, making sure that with each turn only one primitive cell was deposited. All elemental targets had 99.99% purity. The sputtering pressure was set to 2×10^{-3} mbar. With this technique we have fabricated thin-film samples with a precisely set up stoichiometry of $Co_{2.0}Ti_{1.0}Sn_{1.0}$, with errors of <3% for the individual constituents.

All samples used in this study had the following stack sequence: MgO (001)/MgO 5 nm/CTS 18 nm/MgO 2 nm. The lower MgO was deposited by rf sputtering at 2.3×10^{-2} mbar to ensure good crystallinity of the buffer. The upper MgO was deposited by electron-beam evaporation from single-crystal MgO slabs after cooling the samples to less than 100 °C. The base pressure during deposition with the heated substrate was always below 5×10^{-8} mbar.

Resistivity was measured in standard in-line four-probe dc geometry in a closed-cycle He cryostat and a vacuum furnace. The resistivity ρ is calculated from the film thickness d, the voltage U, and the current I as $\rho = d(\pi/\ln 2)(U/I)$. Magnetoresistance was measured using a variable permanent magnet (coaxial Halbach cylinder configuration, Magnetic Solutions Multimag) with a maximum field strength of 10 kOe in the cryostat. The data were taken by driving full magnetization loops and then averaging the points for each field magnitude.

The Seebeck coefficient was determined in a home-built setup in air. The sample was contacted with platinum tips. It was measured at an average temperature of $\bar{T} = 310$ K with a temperature gradient of $\Delta T = 10$ K.

Magnetic measurements were taken using a superconducting quantum interference device (SQUID) at temperatures in the range of 5 to 400 K in magnetic fields of up to 50 kOe.

X-ray diffraction (XRD) and XRR were performed using a Philips X'Pert Pro MPD with a Cu source in Bragg-Brentano configuration. Texture characterization was additionally performed with collimator point focus optics on an open Eulerian cradle.

Temperature-dependent x-ray absorption spectroscopy (XAS), x-ray magnetic circular dichroism (XMCD), and x-ray magnetic linear dichroism (XMLD) were performed at BL 6.3.1 and BL 4.0.2 of the Advanced Light Source (Berkeley, CA). The element-specific magnetic properties were investigated at the Co and Ti $L_{3,2}$ edges in surface-sensitive total electron yield mode[15] for temperatures between 20 and 370 K. For XMCD, the sample was saturated by applying a magnetic field of maximum ±20 kOe along the x-ray beam direction using elliptically polarized radiation with a polarization of $P_{h\nu} = \pm 60\%$ (BL 6.3.1) and $P_{h\nu} = \pm 90\%$ (BL 4.0.2), respectively. The x-ray angles of incidence with respect to the sample surface were $\alpha = 30°$ (BL 6.3.1) and $\alpha = 90°$ (BL 4.0.2), respectively. I^+ and I^- denote the absorption spectra (normalized to the x-ray flux measured by the total electron yield of a Au grid in front of the sample) for parallel and antiparallel orientation of the photon spin and the magnetization of the sample. The XAS and XMCD spectra are defined as $\mathrm{XAS}^c = (I^+ + I^-)/2$ and $\mathrm{XMCD} = (I^+ - I^-)$, respectively. To calculate the element-specific spin and orbital magnetic moments from the data we applied sum-rule analysis;[16] details of the procedure are presented in the Appendix.

Anisotropic XMLD spectra were taken at BL 4.0.2 with 100% linearly polarized light in normal incidence using the eight-pole electromagnet end station.[17] The magnetic field for switching the magnetization of the sample was applied parallel and orthogonal to the polarization vector of the incoming light; the according absorption spectra normalized to the x-ray flux are denoted as $I^{\parallel}$ and $I^{\perp}$. The XAS and XMLD spectra are then defined as $\mathrm{XAS}^l = (I^{\parallel} + I^{\perp})/2$ and $\mathrm{XMLD} = (I^{\parallel} - I^{\perp})$, respectively. Spectra were taken with magnetic fields aligned along the [100] and [110] directions of the Co_2TiSn films. The applied magnetic field of 4.5 kOe was canted out of the surface plane by 10° to improve the electron yield signal. However, the XMLD results are nearly unaffected by this because the demagnetizing field perpendicular to the film plane is so strong that the magnetization is tilted out of plane by less than 5° (measured by analyzing the XMCD asymmetry for different tilting angles).

The XMCD and XMLD spectra were taken by switching the magnetic field at each energy point. To remove nondichroic artifacts we performed measurements for positive and negative polarization (XMCD) or different spatial orientations of the polarization vector (XMLD) and averaged the corresponding spectra.

B. Theoretical approach

The electronic structure probed by x-ray absorption spectroscopy was investigated in direct comparison with *ab initio* electronic structure calculations. We used two different approaches to this end. First, electronic structure calculations were performed with the Munich SPRKKR package, a spin-polarized relativistic Korringa-Kohn-Rostoker method.[18] Second, to take care of the excited-state band structure, which is actually probed in XAS, spectrum simulations were carried out in FEFF9, a relativistic real-space full multiple scattering code.[19]

In SPRKKR, the band structure and the ground-state properties were calculated in the fully relativistic representation of the

TABLE I. Results of band structure calculations with SPRKKR. The magnetic moments are given in μ_B/atom.

$m_{\text{spin}}^{\text{Co}}$	$m_{\text{orb}}^{\text{Co}}$	N_h^{Co}	$m_{\text{spin}}^{\text{Ti}}$	$m_{\text{orb}}^{\text{Ti}}$	N_h^{Ti}
0.96	0.04	2.06	−0.03	0.01	7.65

valence states, thus including spin-orbit coupling. The angular momentum cutoff was set to $l_{\max} = 3$ ($spdf$ basis) and the full potential was taken into account. The bulk lattice parameter of $a = 6.07$ Å was used. The exchange-correlation potential was modeled by the GGA in the Perdew-Burke-Ernzerhof parametrization.

The resulting atomic magnetic moments were then used as input parameters to FEFF9, which is not spin self-consistent. The self-consistent potential was obtained on a cluster of 59 atoms, and the x-ray absorption near-edge structure was calculated on a cluster of 229 atoms. The complex Hedin-Lundqvist self-energy was applied and the calculations were made with the final state rule, including a full screened core hole on the absorber. The angular momentum for the full multiple scattering was taken to $l_{\max} = 3$.

The ground state described by the SPRKKR calculation is not half-metallic with the experimental lattice parameter, in contrast to calculations with full potential linearized augmented plane-wave codes.[1,8] The Fermi energy is slightly above the minority spin gap; a small increase of the lattice parameter would move E_F into the gap. However, this does not significantly change the shape of the calculated XAS spectrum. The total spin moment is 1.9 μ_B/f.u. and the total orbital moment is 0.09 μ_B/f.u. The atom-resolved magnetic moments and the numbers of holes for Co and Ti are given in Table I. The negative Ti spin moment indicates a weakly ferrimagnetic behavior of CTS.

II. EXPERIMENTAL RESULTS

A. Structure

XRD and XRR were utilized to investigate the structure of the films. Figure 1 displays a set of data that were extracted from the measurements. As is clearly visible in Fig. 1(a), the films show Laue oscillations on the (002) reflection that become more pronounced with increasing deposition temperature. Laue oscillations are only observed if the crystalline coherence is very good and the roughness is small. While the two films deposited at lower temperatures show only weak oscillations, the two films deposited at higher temperatures exhibit pronounced fringes. Only weak asymmetry of the fringes is observed for $T_S = 700\,^{\circ}$C, indicating nearly homogeneous (or no) strain along the growth direction.

Four intense (111) reflections were observed in pole figure analysis at the expected tilt angle of $\Psi = 54.74^{\circ}$ for all samples. The intensity increases considerably with increasing deposition temperature. The epitaxial relationship is Co_2TiSn [100] ∥ MgO [110], which is commonly observed for Heusler compounds on MgO (001) substrates.

The out-of-plane lattice parameter c measured on the (004) reflection, displayed in Fig. 1(d), is found to increase with increasing deposition temperature and converges for the highest deposition temperatures. For 700 °C, we find a lattice parameter of $c = 6.105$ Å.

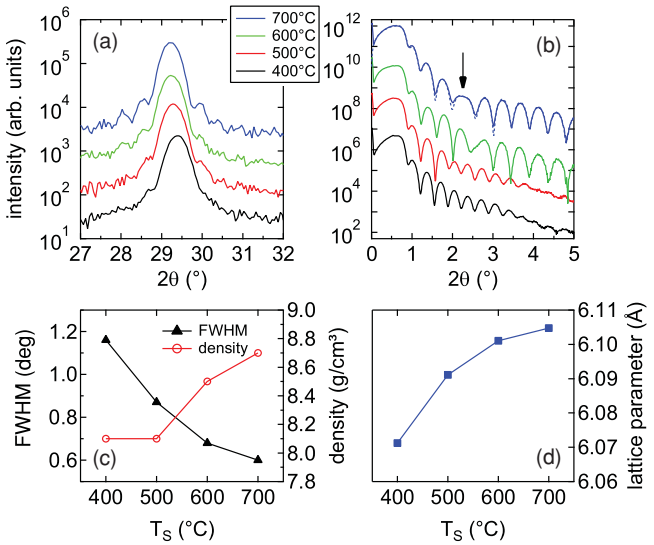

FIG. 1. (Color online) (a) X-ray diffraction scans of the (002) reflections showing Laue oscillations. (b) X-ray reflectometry (XRR) scans. The dashed line represents the best fit to the experimental curve with $T_S = 700\,^{\circ}$C. (c) Full widths at half maximum (FWHM) of the rocking curves and effective density determined by XRR. (d) Out-of-plane lattice parameter c.

The full width at half maximum (FWHM) of the rocking curves measured on the (004) reflections are displayed together with the density determined by XRR in Fig. 1(c). For high deposition temperature the rocking curve FWHM is found to be as low as 0.6°, which demonstrates the narrow orientation distribution of the individual film grains.

XRR provides indirect information on the film morphology. The density determined by XRR has to be seen as an effective density, which only reflects the real film density if the surface roughness is low with a Gaussian distribution on a small lateral scale. In Fig. 1(b), we present the XRR curves of our samples. The roughness is high for the two samples with lower growth temperature, which is identified by a quick vanishing of the Kiessing fringes. The MgO cover layer does not show up as an individual resonance. We find an increase in the XRR density for deposition with 600 °C and more, while the roughness is greatly reduced and the MgO cover layer becomes visible (see arrow). The XRR roughness of the film with $T_S = 700\,^{\circ}$C is 0.3 nm. The scans for the two lower deposition temperatures cannot be fit with the Parratt algorithm.[20] They show two main Fourier components at 18 and 23 nm and a difference component at 5 nm; a columnar growth with high and low grains that have 18 ± 5 nm thickness can be inferred. At higher temperatures, the growth changes to a mode with large and smooth grains of equal height. This behavior has been confirmed by atomic force microscopy.

From Thornton's model[21] of film growth for sputtered films it is expected to find a transition from a fine-grained columnar structure to a regime with large grains governed by bulk diffusion and recrystallization at about half the melting temperature, $T_S/T_m \approx 0.5$. In fact, the melting point

of Co_2TiSn is 1720(20) K;[22] that is, this transition is expected around 600 °C.

Using the experimental bulk lattice parameter $a = 6.07$ Å, the density of the compound is calculated to be 8.446 g/cm^3. If one assumes a perfect, strained epitaxial growth on the MgO substrate, the lattice will be distorted tetragonally, with an in-plane lattice parameter $a = \sqrt{2} \times 4.21 = 5.95$ Å and accordingly expanded out of plane. If the volume remained constant, the out-of-plane lattice parameter would be 6.32 Å. For the film deposited at 700 °C, we measured $c = 6.105$ Å. Recalculating the density for this tetragonal configuration gives $\rho = 8.74$ g/cm^3, which is in close agreement with the measured density of $\rho = 8.7$ g/cm^3. This result supports the growth model discussed above. Furthermore, we have shown in a recent paper by *ab initio* theory that a tetragonal distortion of Co_2TiSn can easily occur because of the low energy associated with the distortion.[8] It is of the order of 50 meV/f.u. and is thus easily activated during the growth. However, at lower temperatures this constitutes a metastable state.

A detailed analysis of the chemical order in the films was performed using anomalous x-ray diffraction. The results from this study will be published elsewhere in detail. The main result is, however, that the atomic disorder decreases considerably with increasing deposition temperature and that the films deposited at 700 °C have a high degree of $L2_1$ order.

B. Magnetism

Measurements taken on the sample with $T_S = 700$ °C give a magnetic moment of $m = 1.6(1)\,\mu_B$/f.u. and a Curie temperature of $T_C = 375(5)$ K (Fig. 2). The Curie temperature is higher than in bulk samples, where it has been reported to be about 355 K. The coercive field is 160 Oe at 20 K and 150 Oe at room temperature. Since the magnetization declines sharply at T_C, we can conclude that the films consist of a single magnetic phase.

C. Electronic transport

Resistivity and magnetoresistance were measured on a sample deposited at $T_D = 700$ °C; the data are shown in Fig. 3. The resistivity shows clearly the cusp-type resistivity anomaly that is also observed for bulk samples of Co_2TiSn at T_C. Details of the transition can be found by analyzing the first and second derivatives of the resistivity curve.

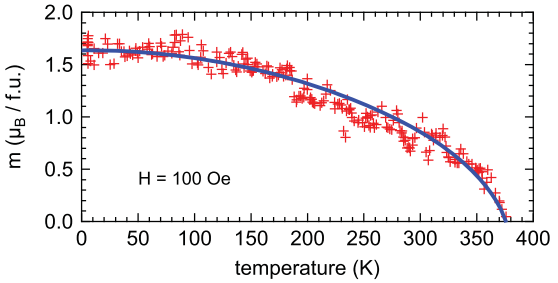

FIG. 2. (Color online) Magnetization in dependence of the sample temperature (markers). It was taken as a temperature sweep with a constant field of 100 Oe. The solid line is a guide to the eye.

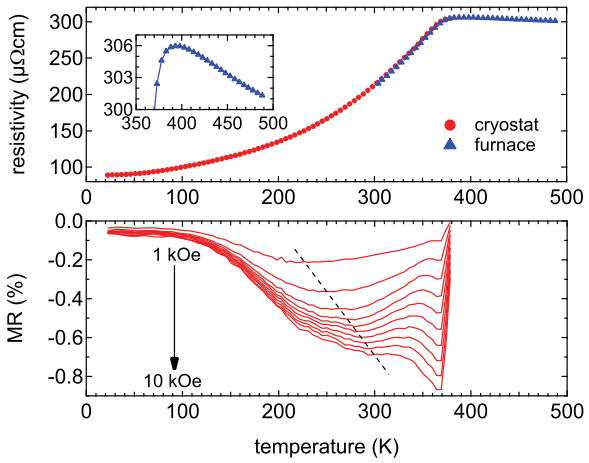

FIG. 3. (Color online) (top) Resistivity of a Co_2TiSn film deposited at $T_S = 700$ °C on a MgO single crystal. The inset shows the region around the ferrimagnet-paramagnet transition. (bottom) Corresponding magnetoresistance for fields of 1 to 10 kOe with the magnetic field $\vec{H}$ in the sample plane and the current $\vec{j} \perp \vec{H}$.

The onset of the transition is defined as the first inflection point of the resistivity; it is found at 350(5) K. The maximum of the resistivity is at 395(5) K (i.e., 20 K above T_C). The offset of the transition, given by the second inflection point, is at 440(5) K. At $T_C = 375(5)$ K, we find the maximal change rate of the resistivity's slope, identified by a clear minimum of the second derivative.

By plotting the logarithm of the resistivity against $1/T$ for the data points above the second inflection point, we find the effective gap width of the paramagnetic state to be $E_g = 6.5 \pm 0.5$ meV. This is considerably smaller than the gap width of 12.7 ± 1 meV reported for bulk samples. However, it was argued by Barth *et al.* that an actual transition to a semiconductor is improbable. They found significant differences for the calculated conductivity tensors between spin-polarized and unpolarized calculations. By mixing the states weighted by a molecular field approximation for the magnetization, they could partly explain the anomalous behavior of the resistivity.[10]

Compared with bulk samples, we also find a notably lower residual resistivity $\rho(20\text{K}) = 89\ \mu\Omega$ cm and a total resistivity amplitude $(\rho_{\max} - \rho_{\min}) = 216\ \mu\Omega$ cm, compared to 310 and 205 $\mu\Omega$ cm,[11] or 245 and 135 $\mu\Omega$ cm,[10] respectively. The residual resistivity of a metal is mainly given by its defect density (i.e., dislocations, disorder, impurities, and grain boundaries). In a thin film, one has to take the interfacial scattering into account. Our thin films have very low residual resistivity compared to bulk samples, which might indicate that their crystalline properties are superior to those of bulk samples. We attribute this to large, flat grains and good chemical order.

The temperature dependence of the resistivity is well described by a T^2 term up to 180 K, which is mainly attributed to electron-electron scattering. Above 180 K up to the first inflection point, the curve is better fit by a T^3 law. In bulk samples, the parabolic shape of the resistivity curve at intermediate temperatures is less pronounced than in our films. However, the overall shape is in agreement with the curves found by other authors.

The magnetoresistance (MR) of the film, defined by $\mathrm{MR}(H,T) = [\rho(H,T) - \rho(0,T)]/\rho(0,T)$, shows strongly nonlinear behavior. At low temperature only weak MR is found. With increasing temperature an increasing MR is observed, which is negative over the whole temperature range (i.e., the resistivity is lower if a magnetic field is applied). It has a pronounced, nonlinear dependence on the applied magnetic field. With an available magnetic field of 10 kOe, the MR was by far not saturated. A distinct extremum is observed at large fields right below T_C, being the global minimum of the curve at fields larger than 7 kOe. Above T_C the MR vanishes. The appearance of the extremum and its amplitude are in agreement with the data published by Majumdar *et al.*[11] The MR can be explained in terms of spin fluctuations and associated spin-flip scattering: at low temperature, the fluctuations are nearly zero and a small magnetic field is sufficient to saturate the film. With increasing temperature, fluctuations become more important but can be suppressed by enforcing a particular spin orientation in a strong field. This picture is supported by the shift of the first minimum with increasing magnetic field, denoted by the dashed line in Fig. 3. The MR is enhanced at T_C because the spin fluctuations are strongest at the transition temperature and the ferrimagnetic state is stabilized in a large field. Furthermore, the MR has no traceable anisotropic MR contribution: the typical inversion of the MR at zero field for $\vec{j} \perp \vec{H}$ compared to $\vec{j} \parallel \vec{H}$ is missing.

The Seebeck effect has been measured on the same sample as the resistivity. It was $S = -14 \pm 2\ \mu\mathrm{V/K}$ at 310 K, which is about 2.6 times lower than in the bulk ($-37 \pm 2\ \mu\mathrm{V/K}$).[10] This is in agreement with the much lower resistivity of our films compared to bulk samples. Barth *et al.* pointed out that the Seebeck coefficient can be enhanced by scattering on grain boundaries or impurities,[10] which appear to be rarer in the films. However, the Seebeck coefficient is proportional to ν/σ, with the electrical conductivity σ and the thermal conductivity ν. Thus, the lower S value may also indicate a lower heat conductivity of the film.

D. Interfacial chemistry

XMCD and XAS^c measurements were performed at BL 6.3.1 at 20 K and at room temperature (RT) for films deposited on MgO single crystalline substrates ($T_S = 400\,^\circ$C, $500\,^\circ$C, $600\,^\circ$C, $700\,^\circ$C, and postannealed samples).

The Co XMCD signals for different deposition temperatures show two notable trends: the Co magnetic moment, measured at 20 K, and the ratio of the Co XMCD signals measured at RT and at 20 K increase with increasing T_S. This implies that the chemical order improves with increasing substrate temperature, resulting in higher saturation magnetization and higher Curie temperature. That is in agreement with SQUID measurements on the same samples.

At $T_S = 400\,^\circ$C, $500\,^\circ$C, we found multiplet structures on the Ti $L_{3,2}$ edges, which indicate formation of interfacial TiO_2.[23] These structures almost vanish at $T_S = 600\,^\circ$C and are no longer traceable at $T_S = 700\,^\circ$C. The spectral shapes of the XMCD signals on Co and Ti do not change, however; only the amplitude is reduced at lower deposition temperature. The large roughness of the films deposited at the lower temperatures leads to an incomplete covering with the protective MgO layer. The CTS compound is thus oxidized in air, which is particularly observed as surfacial TiO_2, which is not magnetic.

In vacuum, postannealed samples were additionally investigated for their interfacial chemistry. Annealing at temperatures above $350\,^\circ$C resulted in formation of interfacial TiO_2. Naturally, this also happens at the lower interface to the MgO substrate. Because of the high-growth temperatures, we can expect an oxide thickness of several nanometers. This effect may account for the low average magnetization measured in the SQUID. An oxidized bottom layer of 3 nm thickness can account for the deviation from the nearly 2 μ_B/f.u. measured in the bulk and predicted theoretically.

Using the results from this systematic analysis, we chose two samples for in-detail investigations described in the next section.

E. Element-specific magnetization

Highly resolved XMCD and XMLD spectra were taken at BL 4.0.2 at 20 K for the samples deposited at $400\,^\circ$C and $700\,^\circ$C, respectively (see Figs. 4 and 5). Whereas the XAS^c spectra show significant differences for the two deposition temperatures for Co and Ti, the shape of the XMCD spectra does not depend on the deposition conditions. For Co the deposition at higher temperature results in a more pronounced fine structure, consisting of a double peak at the L_3 resonance and a shoulder about 4 eV above the resonance. These structures are also reflected in the L_2 resonance but are less pronounced. Klaer *et al.* investigated Co_2TiSn bulk samples (*in situ* fractured in UHV for XMCD investigation).[24] They also observed a double-peak structure at the L_3 resonance, but it was less pronounced compared to our sample deposited at $700\,^\circ$C. Moreover, the double peak structure at the L_2 edge was not found in these bulk samples. Yamasaki *et al.*[25] also investigated bulk samples (*in situ* scraped in vacuum for

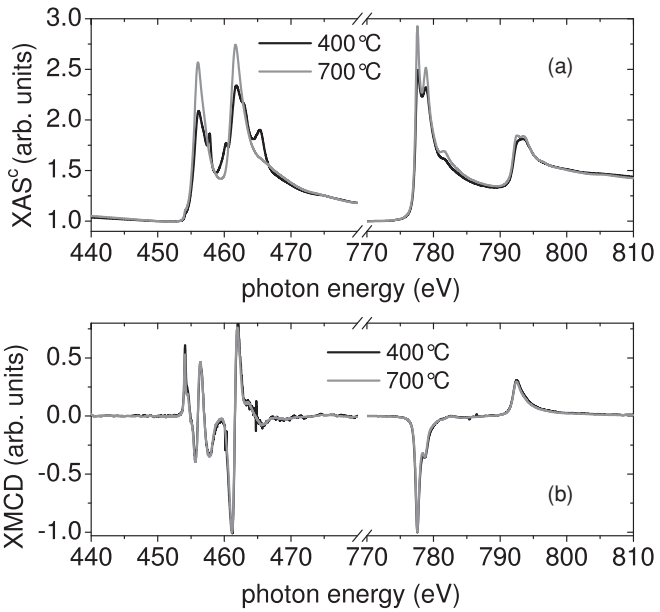

FIG. 4. Normalized XAS^c and XMCD spectra of Ti and Co measured at 20 K for samples deposited on MgO single crystals at $400\,^\circ$C and $700\,^\circ$C, respectively.

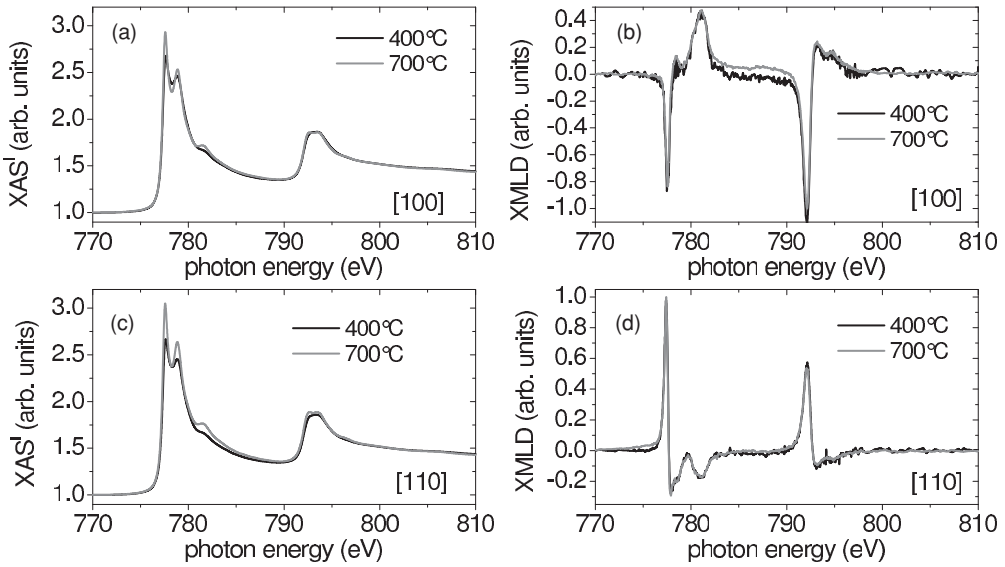

FIG. 5. Normalized XAS^l and XMLD spectra of Co measured at 20 K in the (a and b) [100] and (c and d) [110] directions for samples deposited on MgO single crystals at 400 °C and 700 °C, respectively.

XMCD investigation), but in contrast to the results by Klaer *et al.* and us, they observed three separated peaks at the L_3 edge and only one broad peak at the L_2 resonance. Obviously, their samples had a different electronic structure.

Our Co XMCD spectra also show the double-peak structure at the L_3 edge, while at the L_2 edge only a shoulder is visible. Again, the structures in our XMCD spectra are sharper than those given by Klaer *et al.* and Yamasaki *et al.* Our Ti XMCD spectra shown in Fig. 4(b) are similar to the data by Klaer *et al.*; Yamasaki *et al.* did not provide data on the Ti L edges. However, the shape is very different compared to data collected by Scherz *et al.*[26] on the system Fe/Ti/Fe (110). Therefore, the relative alignment of the Co and Ti magnetic moments is not obvious from a comparison with their reference data.

To get further insight into the element-specific magnetic properties, we applied the XMCD sum rules, which give information on the magnitude and sign of the element-specific spin and orbital moments and the number of d holes. Details of the procedure can be found in the Appendix. The results of the sum-rule analysis for the Co XMCD spectra are summarized in Table II.

The Co spin moment is close to 1 μ_B for a deposition temperature of 700 °C. For the deposition at 400 °C, the Co spin moment is a factor of 2 smaller, but the orbital-to-spin-moment ratio is nearly identical for both deposition temperatures; the orbital moment is parallel to the spin moment. Both spin and orbital moments are in very good agreement with the theoretical results. The number of d holes is lower than for pure Co metal (1.75 and 1.5 for Co_2TiSn deposited at 700 °C and 400 °C, respectively, and 2.4 for pure Co[27]), which indicates a rather large charge transfer to the Co d states in Co_2TiSn. It is actually even a bit lower than the theoretical value of 2.06.

TABLE II. Results of the sum-rule analysis of the Co XMCD spectra measured at 20 K for the samples deposited at 400 °C and 700 °C, respectively.

T_S	m_{spin}	m_{orb}	m_{orb}/m_{spin}	N_h
400 °C	0.48 μ_B	0.025 μ_B	5.2%	1.50
700 °C	0.98 μ_B	0.055 μ_B	5.6%	1.75

While the sum rules work well for Co, dynamical screening effects of the x-ray field prohibit their direct application to the early 3d transition metals.[28] This core-hole-photoelectron interaction leads to an intermixing of the L_3 and L_2 resonances, which is the reason for the deviation from the statistical branching ratio of 2 : 1 for the two edges. The intermixing, also known as jj mixing of the $2p_{1/2}$ and $2p_{3/2}$ levels, leads to wrong results when the sum rules are applied to the early 3d transition metals. It was suggested by Scherz that one can estimate the Ti spin moment by multiplying the result from the sum rule analysis by a factor of 4.[27] This result has been obtained on the Fe/Ti/Fe (110) trilayer system. However, it must be expected that this correction factor itself depends on the actual electronic structure and thus the screening strength. The direct result from the sum rule analysis is $m_{spin} = -0.038\,\mu_B$ for the sample deposited at 700 °C, which is in good agreement with the theoretical result. In particular, an antiparallel alignment with the Co spin moment is found. It is worth mentioning that the Ti orbital moment (the apparent value is $m_{orb} = 0.022\,\mu_B$) is aligned antiparallel to the Ti spin moment. The latter is in accordance with Hund's rules, which expect an antiparallel alignment of the spin and orbital moment, because the Ti 3d shell is less than half filled. Because of the formation of interfacial TiO_2, the XMCD data cannot be quantified for $T_S = 400$ °C. However, all qualitative conclusions with respect to the alignment of the Co and Ti orbital and spin moments are preserved for lower deposition temperatures, because the shapes of the Co and Ti XMCD spectra do not depend on T_S. In summary, the XMCD results are in very good agreement with theoretical expectations.

In general, it is expected that the XMLD signal is proportional to the square of the total magnetic moment of the individual atoms (XMLD $= \beta_l \langle m_{total} \rangle^2$), whereas the XMCD

signal should be directly proportional to the magnetic moment (XMCD $= \beta_c \langle m_{\text{total}} \rangle$).[29] Comparing the XMCD and XMLD signals (normalized to the postedge jump height η, because the number of $3d$ holes N_h is different for the samples deposited at 400 °C and 700 °C, respectively) for Co, it is interesting to note that XMLD/XMCD^2 is about 65% larger for the sample deposited at 400 °C than for the 700 °C sample. In the simple picture that the proportionality factors β_c and β_l are the same for both deposition temperatures, this means that in the disordered 400 °C sample some of the Co atoms are antiferromagnetically coupled to the other Co atoms. However, it is known that the XMLD effect can become quite large in systems with localized electrons. The magnitude of the XMLD is given essentially by the magnetic moment and the $2p$-level exchange splitting, which itself is proportional to the magnetic moment. Actually, without the exchange splitting of the $2p$ levels, the XMLD would vanish. Localized $3d$ electron states increase the $2p$-$3d$ exchange interaction, giving rise to an enhanced XMLD.[30] Therefore, the decrease of XMLD/XMCD^2 with the deposition temperature could also hint to a higher degree of localization of the Co moments for the 400 °C sample. This is in agreement with an oxidized surface, in which the electrons should be more localized. However, the fine structure at the Co L edges becomes more pronounced for higher deposition temperature [see Figs. 4(a), 5(a), and 5(c)], which might indicate a higher degree of localization for higher deposition temperatures. The electron localization would give the Co a more atomic character, and atomic multiplets would become important, giving rise to a fine structure on the x-ray absorption spectrum. However, this would contradict the XMLD result. The maximum amplitude of the XMLD for $T_S = 700$ °C is 5.7% at the Co L_3 edge in the [110] direction. Thus, the Co $3d$ states take an intermediate position between the elemental ferromagnets Co and Fe, that have around 2%, and strongly localized systems like Mn in (Ga, Mn)As, which has about 12%.[30] Obviously, this discrepancy needs to be investigated by direct *ab initio* calculations of the absorption spectra, which is discussed in Sec. III.

For the sample deposited at 700 °C, the XMCD and XMLD effect was studied also at elevated temperatures. The normalized XMCD signals of Co and Ti have the same shape at 20, 300, and 370 K. Furthermore, the Ti XMCD asymmetry changes by the same factor as the Co asymmetry between 20 and 370 K. Therefore, the ratio between the Ti and Co magnetic moments is not significantly changed at elevated temperatures.

The temperature dependence of the XMLD signal was measured for the [110] direction. As shown in Fig. 6, the XMLD signal scales well with XMCD^2, which was also found for other materials like (Ga,Mn)As[30] in accordance with the aforementioned expectation.

III. ELECTRONIC STRUCTURE

As discussed above, the fine structure observed at the Co $L_{3,2}$ edges can have its origin in atomic multiplet effects related to electron localization or simply in the particular (itinerant) electronic structure of Co_2TiSn. The experimental XAS and XMCD spectra are compared to calculations with SPRKKR and FEFF9 in Fig. 7.

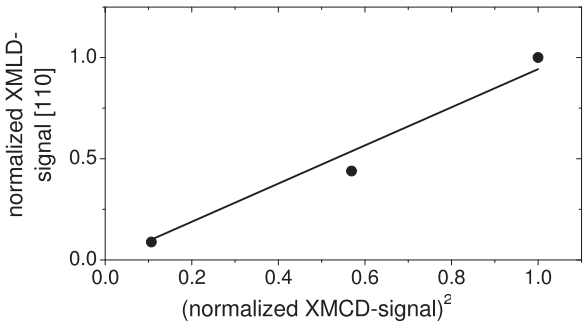

FIG. 6. Normalized Co XMLD signal for the [110] direction as a function of the square of the normalized XMCD signal. The data points correspond to measurements taken at 20, 300, and 370 K. The sample was deposited on MgO single crystals at 700 °C.

The SPRKKR spectra show broad edges and some weak shoulders on the high-energy side of the white lines. The XMCD intensity is significantly too small with respect to the XAS intensity. Furthermore, the ratio of the L_3 and L_2 XMCD signals is incorrect; the L_3 XMCD is too small.

Bekenov *et al.* calculated the XAS/XMCD spectra of CTS *ab initio* using the spin-polarized relativistic linear-muffin-tin-orbital method.[31] Their simulations do not reproduce the double-peak structures and are rather similar to our SPRKKR spectra.

In FEFF9, the SPRKKR spectrum can be principally reproduced when the ground-state density is used. Instead, if the density in the presence of a screened core hole is calculated, we find a structure that is very similar to the experimental spectrum. Because the self-consistency algorithm of FEFF9 is only accurate within 1 eV in its determination of the Fermi

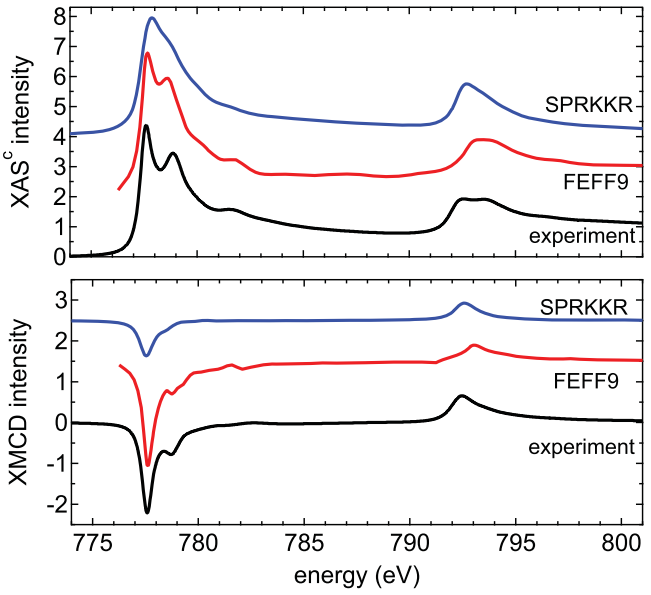

FIG. 7. (Color online) Comparison of the calculated Co $L_{3,2}$ XAS and XMCD spectra carried out in FEFF9 and SPRKKR to experimental spectra. The XMCD signals are scaled to 90% to account for the experimental polarization degree. The experimental and the FEFF9 spectra are scaled to 1 in the postedge region. The SPRKKR spectra are scaled to match the experimental L_3 resonance. The theoretical spectra are aligned in energy with the experimental spectrum.

energy, one can use a small energy shift for fitting, thereby moving E_F within the density of states (DOS). With a shift of -0.2 eV, we obtained the spectrum shown in Fig. 7. Obviously, both the double-peak structure of the white line and the small shoulder 4 eV above the white line are reproduced. Also, the double-peak structure of the XMCD signal is well reproduced. Notably, not only is the shape of the spectrum basically correct, but also the intensities match the experimental data very well. However, the double-peak splitting of the L_3 line is calculated as 1.3 eV, compared to a measured splitting of 1.5 eV.

Since FEFF9 is based on the local density approximation within the density functional theory—and thus relies on single-particle theory—it does not account for atomic multiplet effects, which naturally are many-body effects arising from wave-function coupling. Consequently, we conclude that the features observed in our experimental spectra do not arise from multiplet effects and electron localization. Instead, they are features arising from the excited-state band structure due to the presence of a core hole. This is consistent with the XMLD measurements discussed above, which indicate rather itinerant moments.

Our conclusion is further supported by the analysis given by Klaer *et al.*, who found that the observed structures cannot be explained by charge-transfer multiplet theory.[24] They state that the splitting arises from a nearly pure Co e_g state above E_F, giving rise to the first peak, and from a Co-Ti hybrid state of t_{2g} character, which results in the second peak. Since the t_{2g} states have more itinerant character, the core hole is more screened by the surrounding atoms, while the e_g states are significantly lowered in energy. This core-hole correlation energy ΔE_C was assumed to be 0.5 eV and was confirmed by a measurement on Co_2TiSi. Neglecting the (only weak) energy dependence of the transition matrix elements, and using this core-hole correlation energy and spectral deconvolution, they finally found that the Fermi level of Co_2TiSn is at the edge of the minority valence band; that is, Co_2TiSn would be on the verge of being a half-metal. With the same method, they found that Co_2MnSi has half-metallic character for the unoccupied density of states.

Using the FEFF9 calculations, we can invert this procedure. From *ab initio* calculations, we found the Fermi energy by fitting the experimental spectrum. Now we can use the same Fermi energy and investigate the ground-state DOS calculated by FEFF9. The Co site projected d DOS are shown together with the SPRKKR calculation in Fig. 8. First, we note that the ground-state DOS from FEFF9 and the SPRKKR calculation produce principally the same features, but FEFF9 underestimates the splitting between the bonding and the antibonding states. This is because of the spherical potential approximation and the use of the von Barth–Hedin exchange correlation potential. The unoccupied DOS are, however, in good agreement. Because of finite cluster size effects, the DOS from FEFF9 is broadened. The minority states gap can be identified just below the calculated Fermi level. When comparing the DOS in the presence of the core hole to the ground state, we find that the curve is mainly shifted to lower energies by $\Delta E_C \approx 0.3$ eV. In the unoccupied DOS, this is best seen for the minority e_g peak, which shifts below the calculated E_F. Instead, the Co-Ti t_{2g} peak at 1.4 eV remains essentially unaltered. That is in remarkable agreement with the procedure

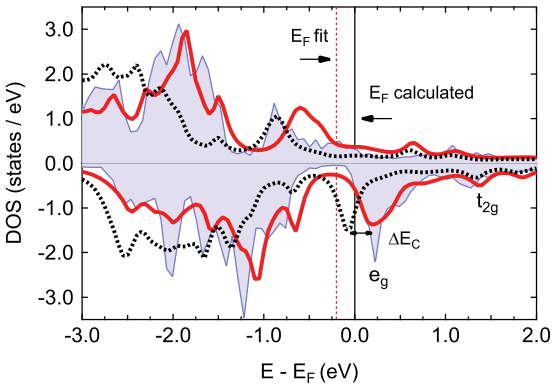

FIG. 8. (Color online) Comparison of the calculated Co site projected d DOS from SPRKKR (shaded blue area) and FEFF9 in the ground state (solid red line) and with an L_3 core hole (dotted black line).

given by Klaer *et al.* When the same Fermi level is applied to the ground-state density as to the excited-state density, we can conclude from our data that Co_2TiSn has half-metallic character with E_F right below the minority valence band (see dotted energy level in Fig. 8).

Finally, we discuss the limitations of our model. As mentioned above, the *ab initio* calculation underestimates the double-peak splitting of the XAS by about 0.2 eV. This introduces an uncertainty in the Fermi energy determination by spectral fitting of the order of the correction itself. With the currently available level of *ab initio* theory this issue cannot be resolved and it remains unclear if Co_2TiSn is a half-metallic ferrimagnet. At least, a full potential treatment would be desirable, and spin self-consistency with more advanced exchange correlation functionals may help to resolve problems with the exchange splitting. However, the SPRKKR calculation finds the t_{2g} peak at slightly lower energy than FEFF9. Thus, it is possible that a more accurate calculation of the XAS requires approaches going beyond DFT.

IV. CONCLUSIONS

We grew thin films of the Heusler compound Co_2TiSn by dc magnetron co-sputtering. Structural investigations revealed highly ordered, fully epitaxial growth of Co_2TiSn thin films on MgO (001) substrates at growth temperatures above 600 °C.

A low residual resistivity supports the conclusion of well-ordered films. The resistivity has a pronounced cusp-type anomaly at T_C. A large magnetoresistance is observed and can be explained in terms of spin fluctuations.

From the XMCD measurements, we find a total magnetization of $1.98 \pm 0.05\ \mu_B$/f.u., where the uncertainty arises from the unknown systematic error in the estimate of the Ti spin moment; the reduced average saturation magnetization of the best film ($T_S = 700$ °C, $m = 1.6(1)\ \mu_B$/f.u.) can be easily explained by an oxidized bottom interface layer of 3 nm thickness.

The results for the element-specific spin and orbital magnetic moments are in quantitative agreement with *ab initio* band structure theory. The fine structures observed for the Co $L_{3,2}$ edges were explained by direct calculations of the XAS using FEFF9. Inclusion of the core-hole potential was

found to reproduce the split white lines. A strong electron localization can be ruled out, in agreement with XMLD results. However, it remains unclear whether Co_2TiSn is a half-metallic ferrimagnet.

ACKNOWLEDGMENTS

The authors gratefully acknowledge financial support by the Deutsche Forschungsgemeinschaft (DFG) and the Bundesministerium für Bildung und Forschung (BMBF). They thank for the opportunity to work at BL 6.3.1 and BL 4.0.2 of the Advanced Light Source, Berkeley, California, USA, which is supported by the Director, Office of Science, Office of Basic Energy Sciences, of the US Department of Energy under Contract No. DE-AC02-05CH11231. They further acknowledge the work of Professor Rehr and his group for developing and providing the FEFF9 code, as well as the work of Professor Ebert and his group for developing and providing the Munich SPRKKR package.

APPENDIX

To calculate spin and orbital moments from the absorption spectra, we applied sum-rule analysis[16] to the XMCD spectra. Thereby, we define the integrals p, q, and r as

$$p = \int_{L_3} (I^+ - I^-) dE, \quad q = \int_{L_3+L_2} (I^+ - I^-) dE,$$
$$r = \int_{L_3+L_2} \left(\frac{I^+ + I^-}{2} - S \right) dE.$$

We used a no-free-parameter two-step-like background function S with thresholds set to the points of inflection on the low-energy side of the L_3 and L_2 white lines and step heights of 2/3 (L_3) and 1/3 (L_2) of the average absorption coefficient in the postedge region ("postedge jump height η") here. Sufficiently far away from the absorption edges and for photon energies above 30 eV, interactions among the atoms in the samples can be neglected[32] and the postedge jump height η is proportional to $\sum_i X_i \sigma_{ai}$, where X_i is the relative concentration of atom i in the sample and σ_{ai} is its total atomic absorption cross section. As pointed out by Stöhr,[33] the number of unoccupied $3d$ states, N_h, is proportional to the integral r via $r = C N_h \eta$. The constant C depends on the transition matrix elements connecting the core and valence states involved in the $2p$-$3d$ transitions and has been analyzed by Scherz for different $3d$ transition metals ($C^{\mathrm{Ti}} = 5.4$ eV, $C^{\mathrm{Co}} = 7.8$ eV).[27] We used the integral r to determine N_h for the different samples. While neglecting the spin magnetic dipole term $\langle T_Z \rangle$ in the XMCD sum rules, the spin and orbital magnetic moments m_{spin} and m_{orb} and their ratio are then given as

$$m_{\mathrm{orb}} = -\frac{1}{P_{h\nu} \cos\theta} \frac{4q}{6C\eta}, \tag{A1}$$

$$m_{\mathrm{spin}} = -\frac{1}{P_{h\nu} \cos\theta} \frac{(6p - 4q)}{2C\eta}, \tag{A2}$$

$$\frac{m_{\mathrm{orb}}}{m_{\mathrm{spin}}} = \frac{2q}{9p - 6q}, \tag{A3}$$

with the elliptical polarization degree $P_{h\nu}$ and the angle θ between magnetization and x-ray beam direction.

*meinert@physik.uni-bielefeld.de

[1] H. C. Kandpal, V. Ksenofontov, M. Wojcik, R. Seshadri, and C. Felser, J. Phys. D **40**, 1507 (2007).
[2] Y. Miura, M. Shirai, and K. Nagao, J. Appl. Phys. **99**, 08J112 (2006).
[3] S. Ishida, S. Akazawa, Y. Jubo, and J. Ishida, J. Phys. F **12**, 1111 (1982).
[4] P. Mohn, P. Blaha, and K. Schwarz, J. Magn. Magn. Mater. **1**, 183 (1995).
[5] I. Galanakis, P. H. Dederichs, and N. Papanikolaou, Phys. Rev. B **66**, 174429 (2002).
[6] S. C. Lee, T. D. Lee, P. Blaha, and K. Schwarz, J. Appl. Phys. **97**, 10C307 (2005).
[7] M. C. Hickey, A. Husmann, S. N. Holmes, and G. A. C. Jones, J. Phys.: Condens. Matter **19**, 2897 (2006).
[8] M. Meinert, J. M. Schmalhorst, and G. Reiss, Appl. Phys. Lett. **97**, 012501 (2010).
[9] P. J. Webster and K. R. A. Ziebeck, J. Phys. Chem. Solids **34**, 1647 (1973).
[10] J. Barth, G. H. Fecher, B. Balke, S. Ouardi, T. Graf, C. Felser, Andrey Shkabko, Anke Weidenkaff, P. Klaer, H. J. Elmers *et al.*, Phys. Rev. B **81**, 064404 (2010).
[11] S. Majumdar, M. K. Chattopadhyay, V. K. Sharma, K. J. S. Sokhey, S. B. Roy, and P. Chaddah, Phys. Rev. B **72**, 012417 (2005).
[12] V. Sharma, A. K. Solanki, and A. Kashyap, J. Magn. Magn. Mater. **322**, 2922 (2010).
[13] P. Gupta, K. J. S. Sokhey, S. Rai, R. J. Choudhary, D. M. Phase, and G. S. Lodha, Thin Solid Films **517**, 3650 (2009).
[14] E. Suharyadi, T. Hori, K. Mibu, M. Seto, S. Kitao, T. Mitsui, and Y. Yoda, J. Magn. Magn. Mater. **322**, 158 (2010).
[15] Y. U. Idzerda, C. T. Chen, H. J. Lin, G. Meigs, G. H. Ho, and C. C. Kao, Nucl. Instrum. Methods Phys. Res. A **347**, 134 (1994).
[16] C. T. Chen, Y. U. Idzerda, H. J. Lin, N. V. Smith, G. Meigs, E. Chaban, G. H. Ho, E. Pellegrin, and F. Sette, Phys. Rev. Lett. **75**, 152 (1995).
[17] E. Arenholz and S. Prestemon, Rev. Sci. Instrum. **76**, 083908 (2005).
[18] The Munich SPRKKR package, version 5.4, H. Ebert *et al.*, [http://olymp.cup.uni-muenchen.de/ak/ebert/SPRKKR]; H. Ebert, in *Electronic Structure and Physical Properties of Solids*, Lecture Notes in Physics Vol. 535, edited by H. Dreyssé (Berlin, Springer, 2000).
[19] J. J. Rehr, J. J. Kas, M. P. Prange, A. P. Sorini, Y. Takimoto, and F. Vila, C. R. Phys. **10**, 548 (2009).
[20] L. G. Parratt, Phys. Rev. **95**, 359 (1954).
[21] J. A. Thornton, J. Vac. Sci. Technol. **11**, 666 (1974).
[22] B. Balke (private communication).
[23] R. Brydson, H. Sauer, W. Engel, J. M. Thomass, E. Zeitler, N. Kosugi, and H. Kuroda, J. Phys.: Condens. Matter **1**, 797 (1989).
[24] P. Klaer, M. Kallmayer, C. G. F. Blum, T. Graf, J. Barth, B. Balke, G. H. Fecher, C. Felser, and H. J. Elmers, Phys. Rev. B **80**, 144405 (2009).

[25] A. Yamasaki, S. Imada, R. Arai, H. Utsunomiya, S. Suga, T. Muro, Y. Saitoh, T. Kanomata, and S. Ishida, Phys. Rev. B **65**, 104410 (2002).
[26] A. Scherz, H. Wende, and K. Baberschke, Appl. Phys. A **78**, 843 (2004).
[27] A. Scherz, Ph.D. thesis, Freie Universität Berlin, 2004.
[28] A. L. Ankudinov, A. I. Nesvizhskii, and J. J. Rehr, Phys. Rev. B **67**, 115120 (2003).
[29] J. Kuneš and P. M. Oppeneer, Phys. Rev. B **67**, 024431 (2003).
[30] A. A. Freeman, K. W. Edmonds, G. van der Laan, N. R. S. Farley, T. K. Johal, E. Arenholz, R. P. Campion, C. T. Foxon, and B. L. Gallagher, Phys. Rev. B **73**, 233303 (2006).
[31] L. V. Bekenov, V. N. Antonov, A. P. Shpak, and A. N. Yaresko, Condens. Matter Phys. **8**, 565 (2005).
[32] A. Thomson *et al.*, *X-ray Data Booklet* (Lawrence Berkeley National Laboratory, Berkeley, CA, 2009) [http://xdb.lbl.gov].
[33] J. Stöhr, J. Electron Spectrosc. Relat. Phenom. **75**, 253 (1995).